The Astrophysical Journal, 705:1160–1172, 2009 November 10 doi:10.1088/0004-637X/705/2/1160

THE *SPITZER* c2d SURVEY OF NEARBY DENSE CORES. VII. CHEMISTRY AND DYNAMICS IN L43

Jo-Hsin Chen[1], Neal J. Evans, II[1], Jeong-Eun Lee[2], and Tyler L. Bourke[3]

[1] Department of Astronomy, The University of Texas at Austin, Austin, Texas 78712–1083, USA; jhchen@astro.as.utexas.edu, nje@astro.as.utexas.edu

[2] Department of Astronomy and Space Science, Astrophysical Research Center for the Structure and Evolution of the Cosmos, Sejong University, Seoul 143-747, Republic of Korea; jelee@sejong.ac.kr

[3] Harvard-Smithonian Center for Astrophysics, 60 Garden St., Cambridge MA 02138, USA; tbourke@cfa.harvard.edu

Received 2009 June 17; accepted 2009 September 23; published 2009 October 19

ABSTRACT

We present results from the *Spitzer Space Telescope* and molecular line observations of nine species toward the dark cloud L43. The *Spitzer* images and molecular line maps suggest that it has a starless core and a Class I protostar evolving in the same environment. CO depletion is seen in both sources, and DCO^+ lines are stronger toward the starless core. With a goal of testing the chemical characteristics from pre- to protostellar stages, we adopt an evolutionary chemical model to calculate the molecular abundances and compare with our observations. Among the different model parameters we tested, the best-fit model suggests a longer total timescale at the pre-protostellar stage, but with faster evolution at the later steps with higher densities.

Key words: ISM: individual (L43, RNO91) – stars: formation

Online-only material: color figures

1. INTRODUCTION

The first step in our understanding of star formation is to determine the properties of dense cores through observations. In general, dust continuum emission is useful to study physical structures of the envelope with tools of radiative transfer modeling. Molecular emission lines are complementary to trace physical properties through studies of excitation; also the line profiles can uniquely probe kinematics. However, the molecular abundances are not homogeneous for all species throughout the core, which easily leads to confusion when interpreting the observed lines. For example, the effect of selective depletion is observed: carbon-bearing and sulfur-bearing molecules are easily depleted in the inner cold, dense region of starless cores, and nitrogen-bearing molecules can remain in the gas phase at higher densities (e.g., Caselli et al. 1999; Tafalla et al. 2002, 2004; Lee et al. 2003). Once a central object forms, the chemistry becomes more complicated since the temperature distribution can be drastically affected by the additional heating mechanisms such as radiation of the central protostellar object and shocks from outflow. The surrounding materials are heated up and reach the evaporation temperature of CO, the main gas-phase repository of carbon. The abundances of other molecules such as HCO^+ and H_2CO can be enhanced by their desorption off dust grains as well as the higher formation rates due to the increase of gas-phase CO abundance. The desorbed CO can also destroy N_2H^+, resulting in a drop in N_2H^+ abundance, and an anti-correlation of $C^{18}O$ and N_2H^+ emission has been seen toward a few Class 0 protostars (e.g., Jørgensen 2004a; Lee et al. 2007) on $\sim 10^3$ AU scale. Such chemical characteristics obtained from molecular spectra can potentially be used to constrain the evolutionary state, but a comprehensive picture of coupled dynamical and chemical evolution is needed since the chemistry depends on not only elapsed time but also density and temperature. Moreover, our knowledge of critical chemical processes, which needs laboratory experiments relevant to interstellar environments, is still limited.

L43 is a Lynds opacity class 6 (i.e., the highest opacity) dark nebula (Lynds 1962) located near the Ophiuchus cloud at a distance of 130 pc (de Geus et al. 1989). A bipolar molecular outflow driven by IRAS 16316−1540 (André & Montmerle 1994) is seen, as well as a circumstellar envelope elongated perpendicular to the outflow axis (Mathieu et al. 1988; Lee et al. 2002; Lee & Ho 2005). The northern outflow lobe is redshifted, and the southern outflow lobe is blueshifted. A reflection nebula RNO91 is associated with the outflow source (Hodapp 1994). Two sources (hereafter RNO91 and L43E) are detected at submillimeter wavelengths (e.g., Ward-Thompson et al. 1999; Shirley et al. 2000; Kirk et al. 2005; Young et al. 2006). It is usually assumed that RNO91 is equivalent to IRAS 16316−1540, and L43E is a starless core. The mass within 3σ contours is estimated to be $0.3 \pm 0.1\,M_\odot$ for the dense core associated with RNO91 and $0.8 \pm 0.2\,M_\odot$ for L43E from the Submillimeter Common-User Bolometer Array (SCUBA) 850 μm observations (Young et al. 2006). The two sources are roughly 80″ apart and provide a test bed for chemical signatures prior to and during collapse.

A few starless cores and cores with central protostars have been previously studied in detail with a combination of modeling and observations. Typically, envelope density and temperature distributions are determined with dust radiative transfer modeling, which provides the inputs for line simulation, and the radial dependence of molecular abundances can be tested. For example, empirical abundance models, such as a step function, are used to describe the amount of depletion in starless cores (e.g., Lee et al. 2003). For sources with central heating, a drop function with the innermost region undepleted can reasonably reproduce the observed lines (e.g., Jørgensen et al. 2004b). Abundance profiles predicted by evolutionary chemical models with varying densities and temperature are also considered; for example, Aikawa et al. (2005) examined the observed properties of four prestellar cores with contracting Bonnor-Ebert (BE) spheres, and Evans et al. (2005) presented line modeling of a collapsing protostar, B335, with a chemical model incorporating inside-out collapse (Shu 1977), described in Lee et al. (2004). In this paper, we also aim at testing such dynamical and chemical models, but L43 provides two snapshots, with and without protostellar heating, which allow us to compare the chemical

behavior at different evolutionary stages based on the same initial environmental condition.

This paper presents new observations of molecular spectra and mid-infrared observations toward L43, and we follow the method of Lee et al. (2004) in attempts to interpret the data, including a dynamical model, continuum radiative transfer, gas energetics, and line radiative transfer. The chemical network is updated with a new binding energy of N_2 (Öberg et al. 2005), and we used the N_2H^+ dissociative recombination rates of Geppert et al. (2004). We have also extended the network to include deuterated species since deuterium fractionation is important. This is especially true in early phases when it is associated with CO depletion. Section 2 describes the observations, Section 3 presents observational results and simple analyses, Section 4 details the modeling sequence, and the modeling results are discussed in Section 5.

2. OBSERVATIONS

2.1. Spitzer Space Telescope

Mid-infrared observations of L43 were performed with the *Spitzer* Infrared Array Camera (IRAC; Fazio et al. 2004) and Multiband Imaging Photometer for *Spitzer* (MIPS; Rieke et al. 2004) aboard the *Spitzer Space Telescope* by the Spitzer legacy Program, From Molecular Cores to Planet-Forming Disks (c2d; Evans et al. 2003). The IRAC observations (Astronomical Observation Request [AOR] ID 0005121280, 0005121792) were obtained in all four bands (3.6, 4.5, 5.8, and 8.0 μm) on 2004 August 16 and 17. Two epochs of observation were taken to allow the identification and removal of the asteroids, each with 10″ dithering, a 12 s exposure, and a 0.6 s of the high-dynamic range (HDR) mode image. The MIPS observations (AOR ID 0009409792, 0009433344) were also taken in two epochs at the first two bands, 24 μm and 70 μm, on 2004 March 10. We integrated one cycle of 3 s for 24 μm, and three cycles of 3 s for 70 μm.

The data were processed with pipeline version S13.2.0 of Spitzer Science Center, and improved by the c2d team with corrections of artifacts. Detailed discussions of the data processing and products by the c2d team are included in the delivery documentation (Evans et al. 2007), as well as in Harvey et al. (2006) on IRAC data and Young et al. (2005) on MIPS data.

Follow-up observations that are significantly deeper than those of c2d were performed as part of Spitzer program 20386 (PI: Philip C. Myers). The observations with IRAC were made on 2005 August 22 (AOR key 14612480), and with MIPS at 24 μm only on 2006 April 8 (AOR key 14617600). For the IRAC observations the on-source time of 480 s (16 dithers of 30 s each) is ten times longer that used for c2d. For the MIPS 24 μm observations the on-source time is 333 s, or about seven times longer than c2d.

Follow-up observations with MIPS at 24, 70 and 160 μm were also performed, as part of Spitzer program 30384 (P.I.: Tyler L. Bourke), on 2007 April 14 (AOR key 18158336). The observations utilized scan map mode in all three bands. The data reductions were carried out as described in Stutz et al. (2007). The MIPS images are 15.′5 × 54″ in size, with exposure times of ∼150 s at 24 μm, ∼90 s at 70 μm, and ∼25 s at 160 μm (these are approximate as the sampling is non-uniform). The resolutions of the observations are ∼ 6″, ∼ 18″, and ∼ 40″ at 24, 70, and 160 μm, respectively.

Table 1
CSO Observing Log

Line	Frequency (MHz)	UT Date	Beam Width (arcsec)	η_{MB}	δv (km s^{-1})
^{12}CO 2–1	230537.970	2005 Mar	33	0.82	0.10
		2006 Jun	32	0.77	0.13
C^{17}O 2–1	224714.400	2000 Jun	33	0.81	0.17
	224714.368[a]	2006 Jun	33	0.77	0.13
C^{18}O 2–1	219560.352	1998 Jul	28	0.57	0.15
		2005 Mar	34	0.82	0.11
		2005 Jun	34	0.74	0.11
		2006 Jun	34	0.77	0.13
CS 7–6	342882.900	2000 Jun	22	0.77	0.10
H_2CO 3_{12}–2_{11}	225697.787	2002 Jun	33	0.59	0.15
		2005 Jun	33	0.74	0.13
HCO^+ 3–2	267557.620	2000 Jun	28	0.81	0.14
		2006 Jun	28	0.77	0.13
DCO^+ 3–2	216112.605	1999 Jul	35	0.60	0.15
		2006 Jun	35	0.77	0.14
N_2H^+ 3–2	279511.701	2003 Jul	27	0.68	0.14
N_2D^+ 3–2	231321.635	2003 Jul	32	0.70	0.13
		2005 Jun	32	0.74	0.11

Note. [a] Reference frequency for the hyperfine shifts in Ladd et al. (1998).

2.2. Molecular Line Observations

Line observations were carried out with the CSO[4] in the period 1998 July to 2006 June. We used a double-side band SIS receiver with an acousto-optical spectrometer (AOS) with a bandwidth of 50 MHz over 1024 channels. The pointing uncertainty was about 3.″6 on average. The observed lines with the reference frequency, the date of observation, the full width at half maximum beam size (θ_b), the main beam efficiency (η_{mb}), and the velocity resolution (δv) are summarized in Table 1. Assuming the source coupling efficiency is unity because the sources are extended, we can calculate the radiation (source) temperature (T_R) given by $T_R = T_A^*/\eta_{mb}$, where T_A^* is the antenna temperature corrected for atmospheric attenuation.

Based on the submillimeter continuum emission mapped with SCUBA (Shirley et al. 2000) at 450 and 850 μm, we use the (0″, 0″) position of ($16^h34^m29^s.0$, $-15°47'3''.2$) in J2000.0 coordinates, and assume that the centroids of RNO91 and L43E are at (7″, 5″) and (89″, 6″), respectively. The observations were performed with position switching at the off position (900″, 0″). All spectra were then reduced with the analysis routines of the package CLASS. Some of the data were taken with different offsets, and in cases with a map, we have synthesized the spectra to the centroid positions at a risk of slight degradation of the spatial resolution.

3. RESULTS

3.1. Source Properties

Figure 1 shows a three-color image of L43 in the IRAC bands 1, 2, and 4. Figure 2 shows the 850 μm contours from Young et al. (2006) on IRAC and MIPS images at the 3.6, 8.0, 70, and 160 μm bands, as well as a 350 μm map from Wu et al. (2007) obtained with the Submillimeter High Angular Resolution Camera (SHARCII) at the CSO. L43E is seen as a dark core at 8.0 μm and is traced well by the 850 μm dust emission. Photometry including the Spitzer results, the submillimeter results, and other observations are listed in Table 2. The table gives the wavelength (λ), flux density (S_ν)

[4] The Caltech Submillimeter Observatory is supported by the NSF.

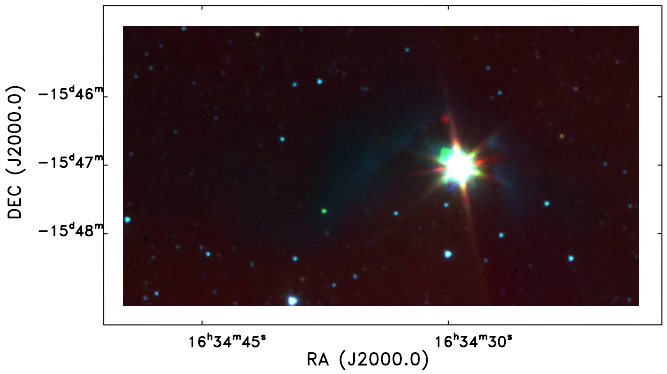

Figure 1. Three-color image composite of IRAC1 (blue), IRAC2 (green); IRAC4 (red) toward L43. The bright object is RNO91, and L43E is the dark region in the east.

with uncertainty (σ), and the aperture size. In cases of no detection, an upper limit is given.

RNO91 falls in the range of Class I sources, as described in Allen et al. (2004) with the IRAC colors [3.6]–[4.5] = 0.93, [5.8]–[8.0] = 0.79. For L43E, there is no point source detected in IRAC or MIPS bands. From all data of RNO91 in Table 2, we also calculate the bolometric luminosity ($L_{\rm bol}$), the bolometric temperature ($T_{\rm bol}$), and $L_{\rm smm}/L_{\rm bol}$, where $L_{\rm smm}$ includes flux at $\lambda > 350$ μm. The $L_{\rm bol}$ is 2.5 ± 0.1 $L_{\odot}$, and $T_{\rm bol}$ is 337.6 ± 18.9 K, which fits the criterion for Class I in Chen et al. (1995). With $L_{\rm smm}/L_{\rm bol} = 0.004$, RNO91 can also be categorized as Class I as defined by André et al. (1993).

3.2. Molecular Lines

Spectra toward the centroid position of both sources are presented in Figure 3. The line parameters derived from the spectra are presented in Table 3, which gives the integrated intensity (I), the velocity with respect to the local standard of rest ($v_{\rm LSR}$), the linewidth (Δv), T_R, and the number of observed positions. For single-peaked lines, these values are determined from a Gaussian fit. For double peaked-lines, T_R is from the stronger peak, $v_{\rm LSR}$ is the velocity of the dip, both determined by eye, I is integrated over the full line, and the Δv is I divided by T_R. For lines with hyperfine structure, $v_{\rm LSR}$ and Δv are from hyperfine structure fitting, I is the total area under these components, and T_R is for the strongest component.

The centroid velocities are estimated to be 0.52 ± 0.01 km s^{-1} for RNO91 and 0.77 ± 0.02 km s^{-1} for L43E from the single peaked lines DCO^+ and $C^{18}O$, which are likely to be optically thin. Figure 4 shows the DCO^+ map in the center region of L43. The velocities are blueshifted toward the east and redshifted toward the west, possibly indicating rotation of the cloud that encompasses both sources. The DCO^+ lines are slightly wider near the RNO91 peak, but no significant variations in linewidths are seen across the mapped region. Figure 5 shows the integrated intensity map of $C^{17}O$ and $C^{18}O$; neither of the two CO isotopologues shows line peaks near the center position of RNO91, which could result from CO depletion, suggesting that the evaporation from central heating is still small. Figure 6 shows the 350 μm contours (Wu et al. 2007) overlaid on the extended DCO^+ integrated intensity map. Several submillimeter peaks are resolved in the 350 μm map, and they lie on the broad extended structure seen in DCO^+, suggesting that they formed from the same structure. CS $J = 2$–1 was mapped by Mathieu et al. (1988) and Lee & Ho (2005) for RNO91 tracing both the outflow and the envelope, but the CS $J = 7$–6 line is not detected in our observations.

Table 2
Observed Flux Densities

Source	λ (μm)	$S_\nu(\sigma)$ (mJy)	Aperture (arcsec)	Reference
RNO91	1.6	250(10)	12	1
	1.65	143(6.86)	2.5[a]	2
	2.17	274(8.34)	2.5[a]	2
	2.2	480(20)	12	1
	3.4	510(20)	12	1
	3.6	737(51.1)	1.7[b]	3
	4.5	1110(66.9)	1.7[b]	3
	5.8	1440(72.0)	1.9[b]	3
	8.0	1660(82.8)	2.0[b]	3
	24	5000(200)[c]	70	4
	70	20300(4060)[c]	70	4
	160	67400(13480)[c]	96	4
	190	38000(15200)	60	5
	350	9900(1600)	40	6
	450	11800(2000)	40	7
	850	1600(90)	40	7
L43E	3.6	< 6.99[d]	1.7[b]	3
	4.5	< 10.17[d]	1.7[b]	3
	5.8	< 57.3[d]	1.9[b]	3
	8.0	< 61.5[d]	2.0[b]	3
	24	< 378[d]	5.7[b]	3
	70	400(80)[c]	70	4
	160	37000(7400)[c]	128	4
	350	6500(1300)	40	6
	450	11400(1900)	40	7
	850	1800(100)	40	7

Notes.
[a] FWHM of 2 Micron All Sky Survey point-spread profile
[b] FWHM of Spitzer point-spread profile
[c] Uncertainty given in c2d delivery documentation (Table 21)
[d] 3σ value estimated with the Sensitivity Performance Estimation Tool (SENSPET) from Spitzer Science Center
References.– (1) Myers et al. 1987; (2) 2 Micron All Sky Survey; (3) results from Spitzer c2d; (4) results from Spitzer Program 30384; (5) Ladd et al. 1991; (6) Wu et al. 2007; (7) Shirley et al. 2000

3.3. Simple Analysis

3.3.1. The H_2 Column Density from Dust Continuum Emission

Assuming the dust grains emit as blackbodies ($I_\nu = \kappa_\nu B_\nu(T_D)$, B_ν is the Planck function), and the emission is optically thin at a submillimeter wavelength, we can relate the observed flux density (S_ν) to the column density of gas ($N(H_2)$) by

$$N(H_2) = \frac{S_\nu}{\mu m_H \kappa_\nu B_\nu(T_D)\Omega},$$

where μ is the mean molecular weight, m_H is the atomic mass, κ_ν is the dust opacity per gram of gas, and Ω is the aperture solid angle. We take the 850 μm data in Table 2 and measure the flux density in an aperture of 34″ to match the main beam size of $C^{18}O$ observations. We adopt the dust opacities from Column 5 of Table 1 in Ossenkopf & Henning (1994, hereafter OH5) for coagulated dust grains with thin ice mantles, and assume a standard gas-to-dust ratio of 100 to get $\kappa_{850} = 0.02$ cm^2 g^{-1}. Assuming T_d of 10 K, we can obtain

$$N(H_2)_{RNO91,S_{850}} = 3.35 \times 10^{22} \text{ cm}^{-2};$$

$$N(H_2)_{L43E,S_{850}} = 4.76 \times 10^{22} \text{ cm}^{-2}.$$

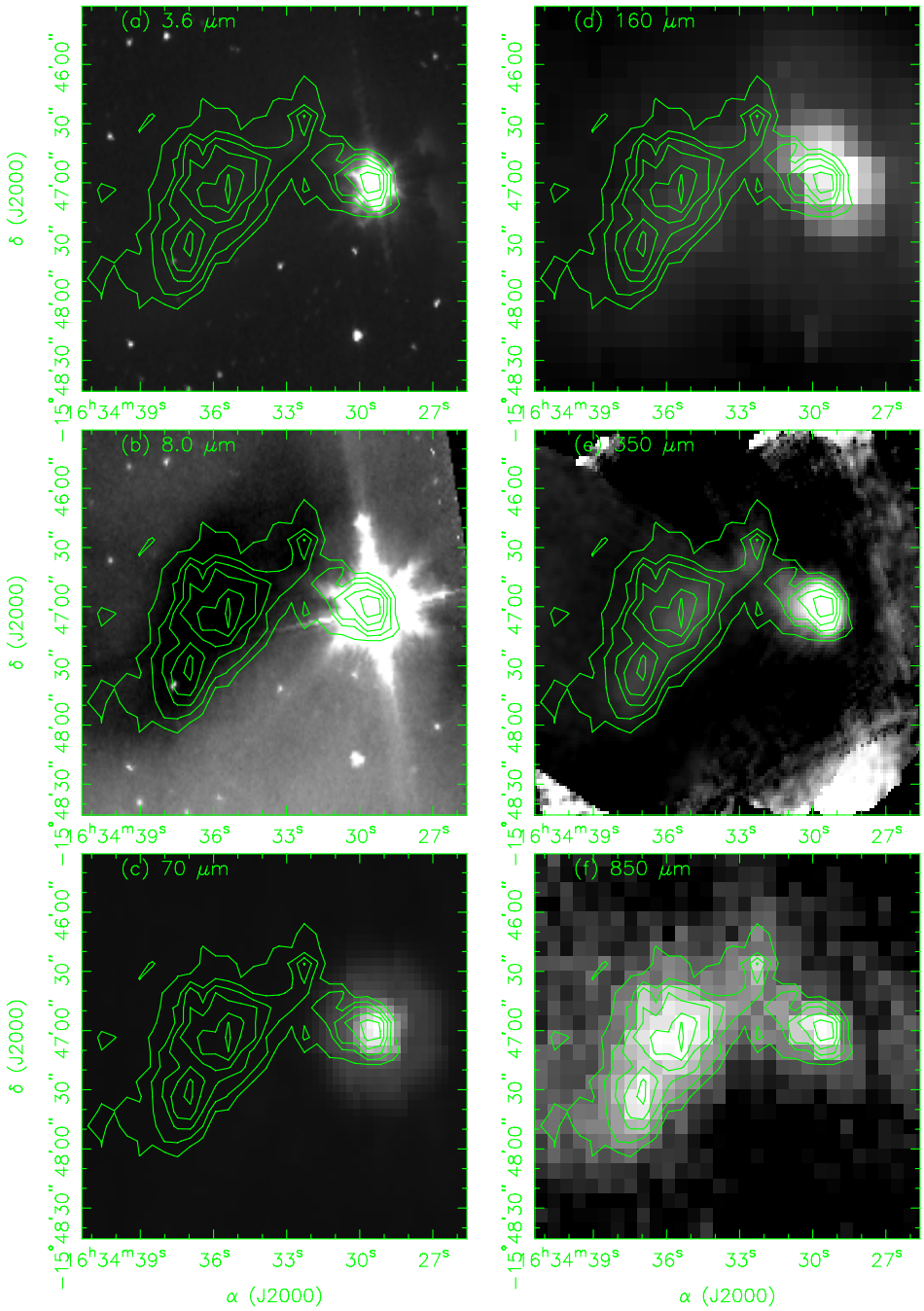

Figure 2. SCUBA 850 μm contours on images at (a) IRAC 3.6 μm from c2d, (b) IRAC 8.0 μm from Spitzer Program 20386, (c) MIPS 70 from Spitzer Program 30384, (d) MIPS 160 μm from Spitzer Program 30384, (e) SHARCII 350 μm, and (f) SCUBA 850 μm.

(A color version of this figure is available in the online journal.)

If T_d is 20K, the calculated $N(H_2)$ would decrease by a factor of 3. If we assume a gas-to-dust mass ratio of ∼124, for example, using the model from Table 4 of Draine (2003, and the references therein), the derived $N(H_2)$ would be 24% higher.

3.3.2. The H_2 Column Density from Molecular Lines

Assuming the line is optically thin and all levels in LTE, the integrated intensity for the transition $J \rightarrow J-1$ of a linear molecule x in $^1\Sigma$ state and the column density ($N(x)$) of species x is given by

$$N(x) = \frac{3kQe^{\frac{E_J}{kT_{\rm ex}}}}{8\pi^3\nu\mu^2 J}\int T_R\, dv$$

as in Equation (2) from Lee et al. (2003), where $E_J = hBJ(J+1)$ in the approximation of rigid-rotor, B is the rotational constant, μ is the dipole moment, Q is the partition function, $T_{\rm ex}$ is the excitation temperature, and T_R is the measured brightness temperature. We can correct this equation for optical depth:

$$N(x)_{\rm thick} = N(x)_{\rm thin}\frac{\tau_\nu}{1-e^{-\tau_\nu}}.$$

We can also convert the column density of a certain molecule into H_2 column density by

$$N({\rm H_2}) = \frac{N(x)}{X(x)},$$

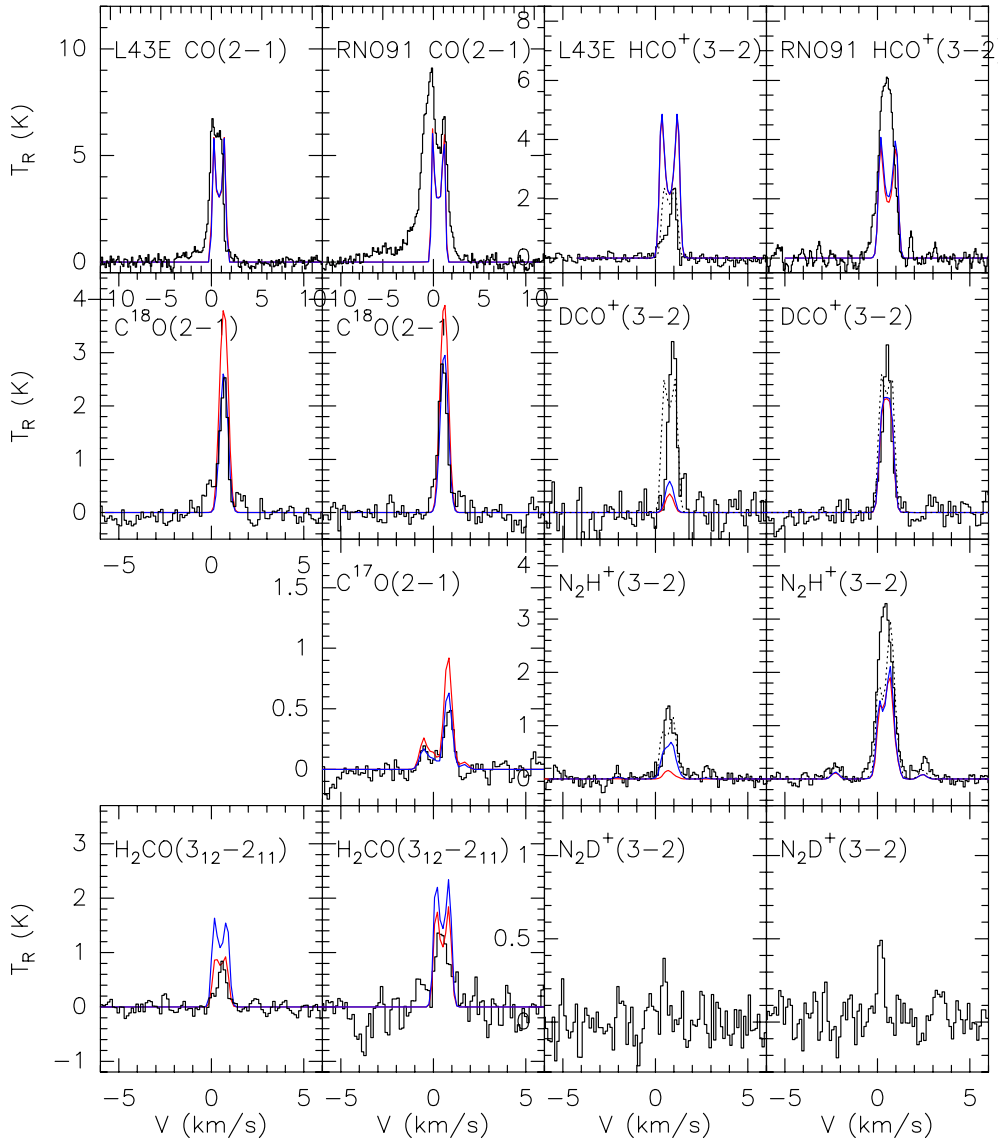

Figure 3. Molecular line observations toward RNO91 and L43E, shown as black solid histograms, and the modeled lines from Model 1 (red lines), Model 2 (blue lines), and empirical models for HCO^+, DCO^+, and N_2H^+ (black dotted lines). Model 2 has a longer timescale for the PPC stage.

where $X(x)$ is the molecular abundance. Under the assumption that all lines are thermalized and $T_{ex} = 10$ K, we calculate $N(H_2)$ using the observed $C^{18}O$ J = 2–1 line averaged over the beam (I in Table 3). We adopt the physical parameters B, μ, and Q from the JPL catalog, $X(CO)$ of 2.7×10^{-4} (Lacy et al. 1994), and $X(CO)/X(C^{18}O)$ ~580 (Wilson & Rood 1994). If $C^{18}O$ is optically thin, we obtain

$$N(H_2)_{RNO91,C^{18}O} = 1.96 \times 10^{21}\ \mathrm{cm}^{-2};$$

$$N(H_2)_{L43E,C^{18}O} = 1.74 \times 10^{21}\ \mathrm{cm}^{-2}.$$

The results are less than one-fifteenth the values calculated from dust emission at 850 μm. A lower X(CO), for example, X(CO) $\sim 1.8 \times 10^{-4}$ from Dickman (1978), can result in less CO depletion, but the ratio of $N(H_2)$ derived from $C^{18}O$ to $N(H_2)$ derived from H_2 would be still less than 0.1 for both sources. Considering that $C^{18}O$ J = 2–1 line might be optically thick, the H_2 column densities derived from the line would be underestimated. To correct the optical depth effect, we can fit the $C^{17}O$ J = 2–1 hyperfine structures to estimate the total optical depth of $C^{17}O$ J = 2–1, and calculate the optical depth of $C^{18}O$ J = 2–1 with the abundance ratio $X(C^{18}O)/X(C^{17}O)$ ~ 4 (Wouterloot et al. 2005). The hyperfine fitting result of $\tau_{C^{17}O(2-1)} \sim 0.59$ for RNO91 has a large error due to the low S/N. After the correction for τ, $N(H_2)$ derived from $C^{18}O$ is still lower than $N(H_2)$ derived by H_2 by a factor of ~10, which strongly indicates the depletion of CO molecules. Furthermore, the column densities derived from $C^{18}O$ are similar in both sources, but from the 850 μm data, the column density is higher in L43E than in RNO91, which suggests there can be more depletion in L43E, with no central heating in the starless core. We can investigate the depletion in more detail through the modeling procedure in the next section where the distribution of excitation temperature and molecular abundances are taken into consideration.

3.3.3. Deuterium Enhancement

At low temperature, the production of H_2D^+ is favored through the exothermic exchange reaction $H_3^+ + HD \rightarrow H_2D^+$

Table 3
CSO Observational Results

Source	Line	$I(\sigma)$ (K km s^{-1})	v_{LSR} (km s^{-1})	Δv (km s^{-1})	T_R (K)	Offset[a] (arcsec)	N_{obs}[b]
RNO91	^{12}CO 2 – 1[c]	22.50(0.19)	0.78(0.10)	2.69(0.08)	7.87(0.21)	(6, 3)	1
	C^{17}O 2 – 1[d]	0.39(0.08)	0.57(0.02)	0.48(0.06)	0.49(0.05)	(7, 5)	169
	C^{18}O 2 – 1	1.71(0.06)	0.51(0.01)	0.59(0.03)	2.74(0.16)	synthesized to (7, 5)	121
	CS 7 – 6	...	...	...	<0.40 (rms 0.11)	(6, 3)	1
	H_2CO $3_{12} - 2_{11}$	1.47(0.19)	0.66(0.06)	1.14(0.21)	1.21(0.27)	(6, 3)	1
	HCO^+ 3 – 2	5.99(0.08)	0.48(0.01)	0.89(0.01)	6.33(0.21)	(0, 0)	1
	DCO^+ 3 – 2	1.85(0.07)	0.52(0.01)	0.59(0.03)	2.92(0.16)	synthesized to (7, 5)	342
	N_2H^+ 3 –2[c]	3.78(0.07)	0.40(0.01)	0.64(0.03)	3.29(0.07)	(7, 5)	11
	N_2D^+ 3 – 2	0.21(0.03)	0.18(0.03)	0.37(0.06)	0.53(0.01)	(7, 5)	5
L43E	^{12}CO 2 – 1	10.10(0.13)	0.46(0.01)	1.38(0.02)	6.88(0.15)	(116, −13)	5
	C^{18}O 2 – 1	1.40(0.09)	0.66(0.02)	0.55(0.05)	2.38(0.18)	(96, −13)	6
	H_2CO $3_{12} - 2_{11}$	0.47(0.04)	0.59(0.03)	0.58(0.07)	0.76(0.01)	(89, 6)	1
	HCO^+ 3 – 2	1.11(0.07)	0.94(0.01)	0.47(0.04)	2.24(0.10)	(89, 6)	5
	DCO^+ 3 – 2	1.65(0.05)	0.88(0.01)	0.50(0.02)	3.13(0.10)	(90, 10)	1
	N_2H^+ 3 – 2[c]	1.19(0.10)	0.73(0.01)	0.23(0.03)	1.36(0.10)	(86, 3)	25
	N_2D^+ 3 – 2	0.11(0.03)	0.48(0.03)	0.26(0.07)	0.39(0.11)	(96, −13)	5

Notes.
[a] (0,0) is the reference position of ($16^h34^m29\overset{s}{.}0$, $-15°47'3\overset{''}{.}2$) (J2000.0), and the centroids of RNO91 and L43E are at (7, 5) and (89, 6), respectively.
[b] Number of observed positions.
[c] Double-peaked line: T_R refers to the stronger peak, v_{LSR} refers to the velocity of the dip, I is of all area, and Δv is I divided by $1.06T_R$ for the Gaussian equivalent linewidth.
[d] Hyperfine structure: v_{LSR} and Δv are from hyperfine structure fitting, I is of all area, and T_R refers the main peak.

+ H_2. The H_2D^+ abundance can be further enhanced with CO depletion, and its deuteration can propagate to other molecules, such as DCO^+ and N_2D^+, by ion–molecule reactions (Dalgarno & Lepp 1984). Therefore, in cold clouds, the molecular D/H ratio can be much higher than the elemental D/H ratio ($\cong 1.5 \times 10^{-5}$; Oliveira et al. 2003).

The integrated intensities of DCO^+(3-2) toward RNO91 and L43E are similar, but the intensity of HCO^+(3–2) is much higher in RNO91 than in L43E, which must be due to the higher HCO^+ column densities and higher gas temperature in RNO91. We do not have optically thin lines such as $H^{13}CO^+$ or $HC^{18}O^+$ to help determine the HCO^+ column densities (e.g., Appendix A1 in Caselli et al. 2002), but we calculate $N(DCO^+)$ and $N(HCO^+)$ for the optically thin case ($\tau_{DCO^+(3-2)} \ll 1$ and $\tau_{HCO^+(3-2)} \ll 1$). For constant abundances and optically thin lines, we obtained $N(DCO^+)_{L43E}/N(HCO^+)_{L43E} \sim 4.11$ and $N(DCO^+)_{RNO91}/N(HCO^+)_{RNO91} \sim 0.85$, assuming $T_{ex} = 10$ K. If T_{ex} is 1 K lower ($T_{ex} = 9$ K), the column densities can increase by 25%–30% for each molecule. The optically thin approximation gives a lower limit of 4.8 for the difference of the enhancement factor $N(DCO^+)/N(HCO^+)$ between L43E and RNO91.

In a CO-depleted region, N_2D^+ can be more enhanced than DCO^+ since it suffers from less depletion. Assuming the N_2H^+ lines are optically thin, $N(N_2H^+)$ toward L43E can be derived to be 1.23×10^{13} cm^{-2}. Also, from Section 3.3.2, the CO depletion factor (f_D) of L43E is ~ 22. From the samples of starless cores in Crapsi et al. (2005), objects with higher N_2H^+ column densities ($> 10^{13}$ cm^{-2}) and more CO depletion ($f_D > 10$) tend to have higher $N(N_2D^+)/N(N_2H^+)$ abundance ratio (> 0.1) and can be recognized as the most evolved starless cores. However, the line intensity of N_2H^+(3-2) toward L43E is ~3 times lower than RNO91 and N_2D^+ (3–2) is only marginally detected in L43E with a very narrow line. The $N(N_2D^+)/N(N_2H^+)$ ratio we derived is ~0.03. For RNO91, the $N(N_2D^+)/N(N_2H^+)$ ratio we derived is ~ 0.02, which is at the lower end compared with the starless core samples because of heating from the central protostar.

4. THE MODELING PROCEDURE

In this section we describe the sequence of modeling from the determination of the dust and gas temperature distribution to line simulation. Similar techniques were employed in Young et al. (2004) and Evans et al. (2005), but in this paper, we apply an updated chemical network.

For a given density structure ($n(r)$), we can calculate $T_D(r)$ by computing the transport of energy through the dust envelope (Section 4.1), and we simulate the observed spectral energy distribution (SED) and the spatial intensity distribution ($I_\nu(b)$, where b is the impact parameter). Then $T_K(r)$ can be calculated from a gas energetics code (Section 4.2). We use an evolutionary model including the self-consistent treatment of dynamics, dust continuum radiative transfer, gas energetics, and chemistry (Section 4.3). Once we obtain the molecular abundances ($X(r)$), we can calculate the populations of relevant energy levels ($n_j(r)$), simulated line profiles, and compare the observations with the simulations (Section 4.4).

4.1. Dust Models

We use the radiative transfer package CSdust3 (Egan et al. 1988), which has input parameters of luminosity of the central source, dust opacity as a function of wavelength, the strength of the interstellar radiation field (ISRF), and the density distribution of the envelope. The program ObsSph (Shirley et al. 2002) then takes the output from CSdust3 and simulates the telescope observations. For simplicity and because of the limitation of one-dimensional model, we focus on the SED fitting at longer wavelengths to trace the envelope. At short wavelengths ($\lambda \leqslant 60$ μm), the SED is more sensitive to opacity and detailed geometry. For example, RNO91 is known to have an inclined disk (Weintraub et al. 1994), and the infrared spectra also show inclination effects, such as silicate emission (e.g., Boogert et al. 2008). With an one-dimensional model envelope, the amount of observed protostellar emission that directly comes through the outflow cavity is not taken into account, which can lead to

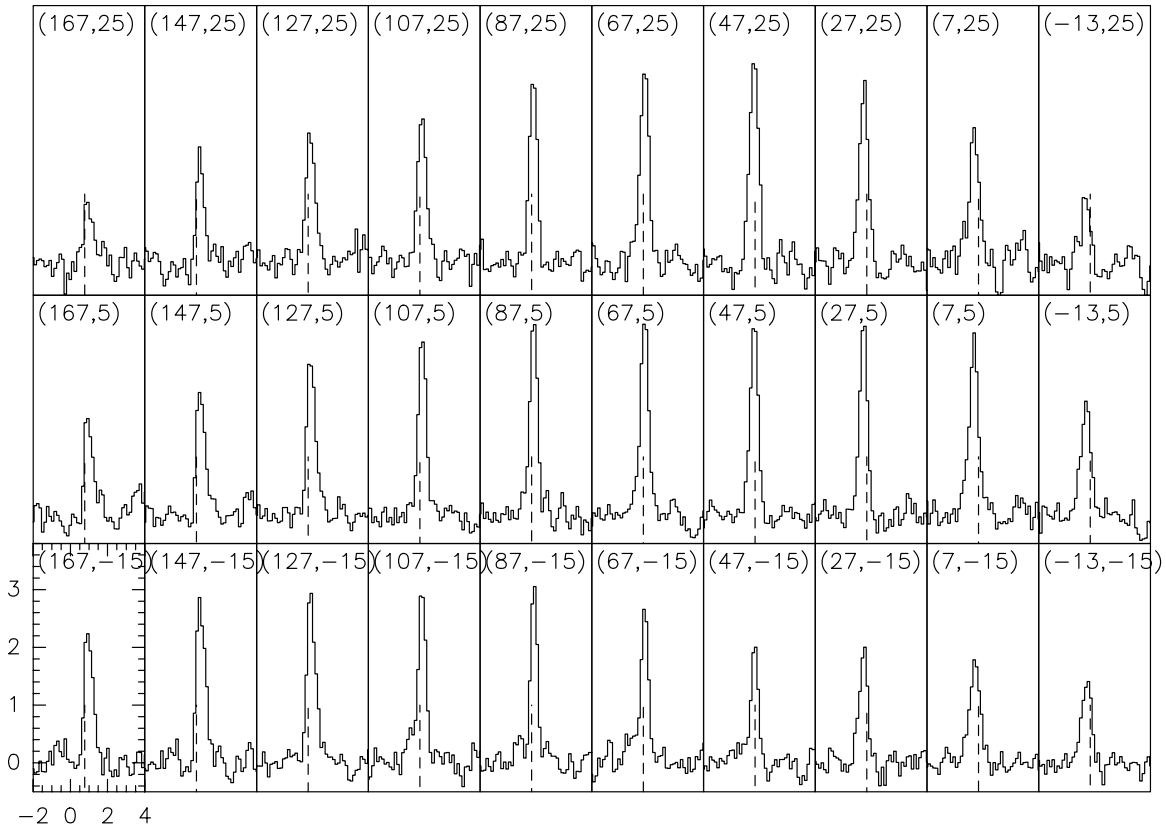

Figure 4. Map of DCO^+(3-2) in the L43 region. The spectra are convolved to the position of RNO91 at (7″, 5″) in 20″ steps. The dashed lines indicate $v_{LSR} = 0.77$ km s^{-1} for L43E at (89″, 6″). The velocities toward the east are redshifted relative to L43E, and the velocities toward the west are blueshifted.

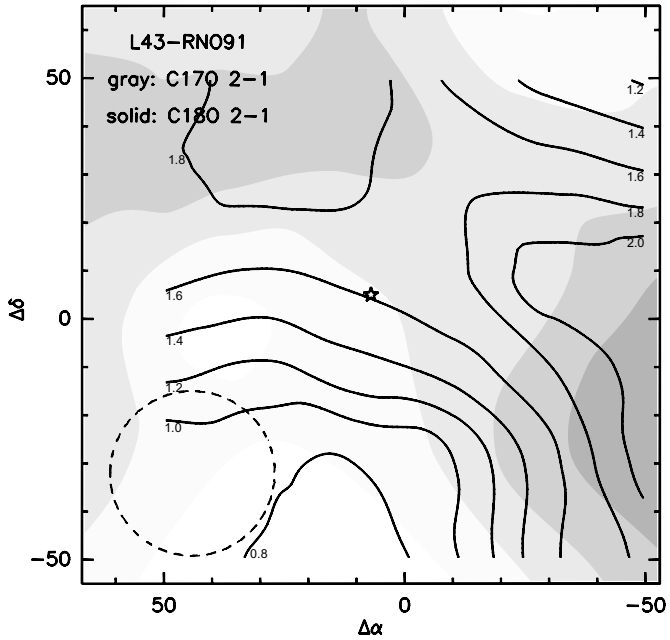

Figure 5. Integrated intensity map of $C^{18}O$(2–1) (solid lines) and $C^{17}O$(2–1) (grayscale) convolved in 30″ steps. The $C^{18}O$ contour levels start at 0.8 K km s^{-1} and increase by 0.2 K km s^{-1}. The $C^{17}O$ contour levels start at 3σ and increase by 2σ. The star marks the position of RNO91, and there is no obvious intensity peak in the mapped region in either line. The $C^{17}O$(2–1) beam is shown in dashed line.

an underestimate of fluxes, particularly at mid-IR wavelengths (e.g., Whitney et al. 2003a, 2003b; Robitaille et al. 2006; Crapsi et al. 2008).

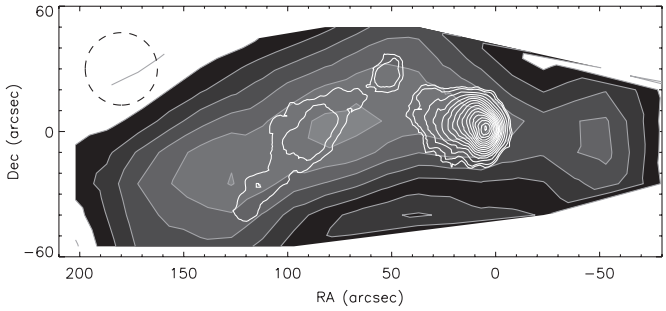

Figure 6. SHARCII 350 μm contours (solid white) overlaid with DCO^+(3-2) integrated intensity map (gray scale). The 350 μm contour levels are 2σ, 3σ, 5σ, and increased by 2σ. The DCO^+ integrated intensity contours start at 3σ and increase by 2σ. The DCO^+(3-2) beam is shown in dashed lines.

We use the ISRF spectrum based on Cosmic Background Explorer (COBE) data from Black (1994) with ultraviolet (UV) wavelengths described in Draine (1978), and modified by dust extinction with the properties in Draine & Lee (1984) assuming an attenuation by an external A_V outside the core we observe. A scaling factor s_{ISRF} is also introduced to increase or decrease the ISRF at all wavelengths except the cosmic background radiation. For dust opacities in cores, we use the model of OH5 dust since it is successful in reproducing the observed SEDs in star-forming cores (e.g., van der Tak et al. 2000; Evans et al. 2001; Shirley et al. 2002). The inner and outer boundary of the models are set as $R_{in} = 80$ AU and $R_{out} = 8000$ AU, which correspond to 0.″6 and 61.″5, respectively, and R_{out} is substantially smaller than the separation of the two sources. To compare with models, the observed $I_\nu(b)$ are calculated from the 850 μm maps (Shirley et al. 2000), and since RNO91 and

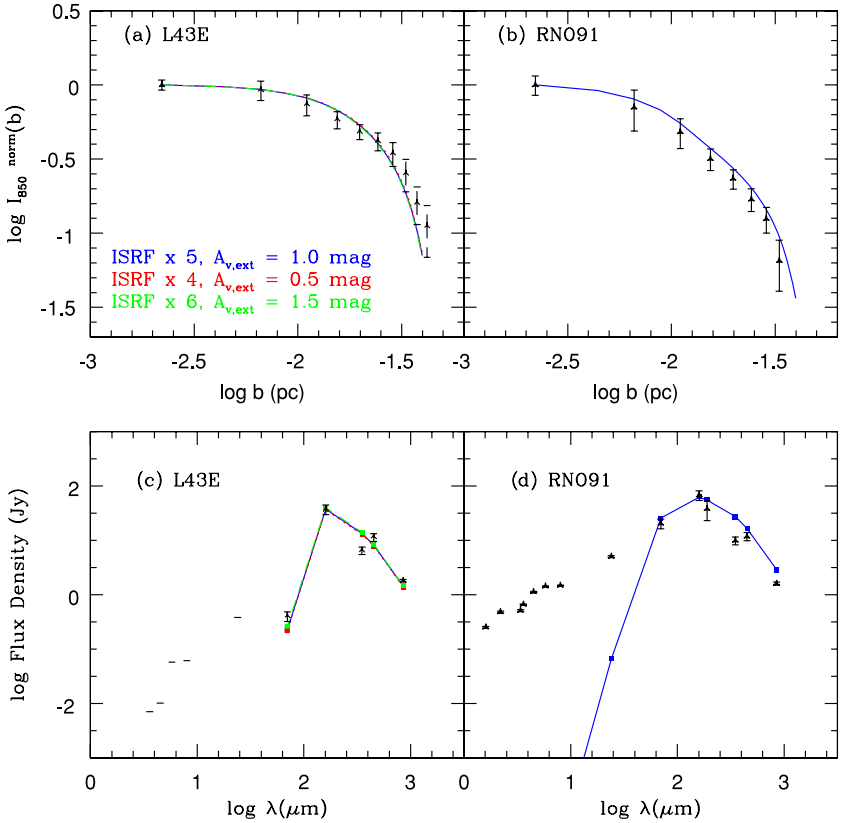

Figure 7. Best-fit dust models for both RNO91 and L43E. (a) and (b) The model fitting of the normalized $I_{850}(b)$; (c) and (d) the SED fitting. The solid blue lines are the model with an external $A_V = 1$ and $s_{\rm ISRF} = 5$, the dotted red lines are the model with an external $A_V = 0.5$ and $s_{\rm ISRF} = 4$, and the dashed green lines are the model with an external $A_V = 1.5$ and $s_{\rm ISRF} = 6$. The different combinations provide similar fits and the modeled lines are on top of each other. The short horizontal lines are marks for the upper limits for L43E from Spitzer Observations.

(A color version of this figure is available in the online journal.)

L43E can be partially overlapping, the data in sectors that are possibly contaminated were excluded. For example, the data in a 90° sector at the east pointing toward L43E are cut out in the averaged $I_\nu(b)$ of RNO91.

Previous observational studies of pre-protostellar cores (PPCs) suggest a region of roughly constant density at small radii (Ward-Thompson et al. 1994), and since they do not have an internal source, the only heating source is the ISRF. We attempt to fit the SED and $I_\nu(b)$ of L43E with a set of BE spheres as discussed in Evans et al. (2001). The central density (n_c) of the BE sphere is mostly determined by comparing the shape of the normalized $I_\nu(b)$. The best-fit values are selected by minimizing χ^2 at 850 μm for $I_\nu(b)$ as well as $\chi^2_{\rm SED}$:

$$\chi^2_{850} = \Sigma\left[\frac{I_\nu^{\rm obs}(b_i) - I_\nu^{\rm mod}(b_i)}{\sigma_I(b_i)}\right]^2 \Big/ N_b,$$

where $I_\nu^{\rm obs}(b_i)$ is the normalized intensity at impact parameter b_i, $I_\nu^{\rm mod}(b_i)$ is the modeled intensity, $\sigma_I(b_i)$ is the uncertainty of the data, and N_b is the number of impact parameters;

$$\chi^2_{\rm SED} = \Sigma\left[\frac{S_{\nu_i}^{\rm obs} - S_{\nu_i}^{\rm mod}}{\sigma_S(\nu_i)}\right]^2 \Big/ N_\nu,$$

where $S_{\nu_i}^{\rm obs}$ is the observed flux, $S_{\nu_i}^{\rm mod}$ is the modeled flux, $\sigma_S(\nu_i)$ is the uncertainty of the data, and N_ν is the number of data points.

To compute $\chi^2_{\rm SED}$, the 350 μm flux is excluded because the observing mode of SHARCII used for these observations tends to lose flux for extended sources (Wu et al. 2007). The 160 μm emission is very sensitive to temperature and is used to constrain the ISRF. We tested models with the external A_V in a range between 0.5 and 5.5 and $s_{\rm ISRF}$ between 1 and 10. Figure 7 shows the best-fit model with a BE sphere of $n_c = 3\times10^5$ cm^{-3}, $s_{\rm ISRF} = 5$, and the external $A_V = 1$. $\chi^2_{\rm SED}$ for the best-fit model is 7.5 (the blue lines in Figure 7), but different combinations of external A_V and $s_{\rm ISRF}$ can provide similar fits, for example, the model with $s_{\rm ISRF} = 4$ and the external $A_V = 0.5$ (red lines in Figure 7) and the model with $s_{\rm ISRF} = 6$ and the external $A_V = 1.5$ (green lines in Figure 7) have $\chi^2_{\rm SED}$ about 15. The external A_V can be further constrained by line modeling of CO(2–1) emission since photoelectric (PE) heating is sensitive to the surrounding extinction, as detailed in Section 4.2.

For the density distribution of RNO91, we use the gravitational collapse model presented by Shu (1977). In this picture, the model begins from an idealized singular isothermal sphere with an envelope with $n(r) \propto r^{-2}$. Collapse begins inside the sphere, and a wave of infall propagates outward at the speed of sound as time progresses. The density inside the infall radius ($r_{\rm inf}$) approximates $n(r) \propto r^{-1.5}$ as material falls into the center. For RNO91 at $\lambda \geqslant 60$ μm, $L_{{\rm bol},\lambda\geqslant60\ \mu{\rm m}} = 0.8\ L_\odot$. The best-fit model adopting this scenario is shown in Figure 7, with an internal heating source of 0.4 $L_\odot$ and $r_{\rm inf}$ of 0.006 pc.

4.2. Gas Energetics

Deep inside the cloud, the gas temperature is equal to the dust temperature because high densities produce rapid collisions between dust and gas. However, at lower densities, since dust

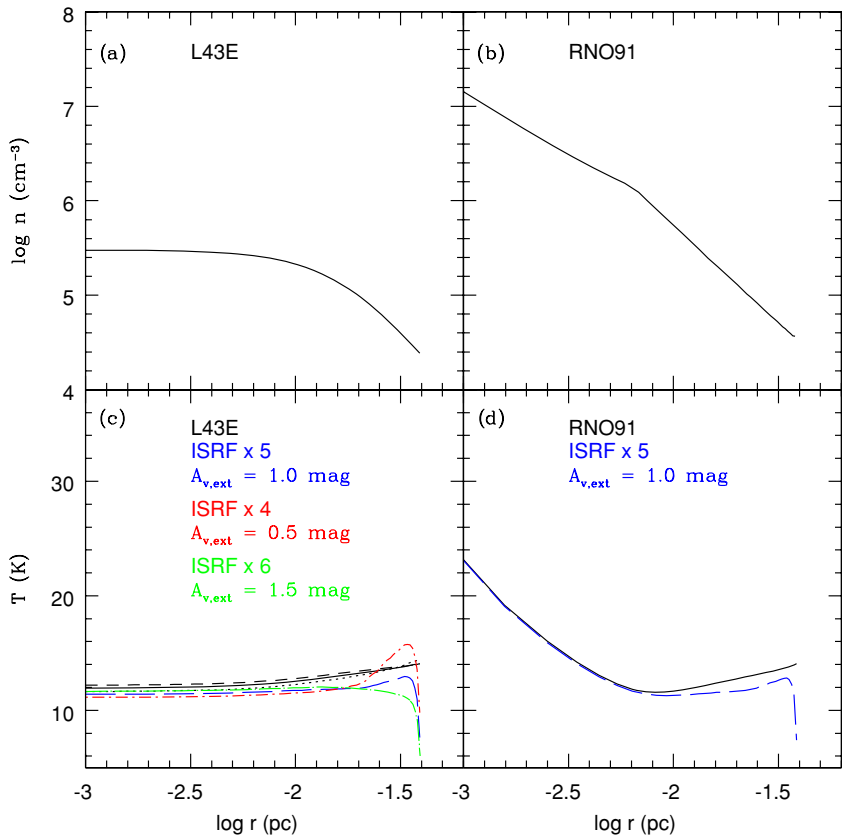

Figure 8. Density profiles and calculated T_D and T_K with the same models in Figure 5. (a) The density profile of BE sphere with $n_c = 3 \times 10^5$ cm^{-3}; (b) the density profile of inside-out collapse model with $r_{\rm inf} = 0.006$ pc; (c) and (d) calculated T_D and T_K. The solid black lines are $T_D(r)$ from the model with $s_{\rm ISRF} = 5$ and $A_V = 1$, the dashed black line is $T_D(r)$ from the model with $s_{\rm ISRF} = 4$ and $A_V = 0.5$, the dotted black line is $T_D(r)$ from the model with $s_{\rm ISRF} = 6$ and $A_V = 1.5$, the long-dashed blue lines are $T_K(r)$ from the model with $s_{\rm ISRF} = 5$ and $A_V = 1$, the dot-short-dashed red line is $T_K(r)$ from the model with $s_{\rm ISRF} = 4$ and $A_V = 0.5$, and the dot-long-dashed green line is $T_K(r)$ from the model with $s_{\rm ISRF} = 4$ and $A_V = 1.5$

(A color version of this figure is available in the online journal.)

and gas are decoupled, the gas temperature must be determined by balancing heating and cooling rates. We use a gas-dust energetics code by S. Doty including gas-dust energy transfer, cosmic ray heating, PE heating, and molecular cooling (details are given in Doty & Neufeld 1997 and the appendix in Young et al. 2004). CO is the major coolant in clouds, and in principle we should include CO depletion in the modeling loop since it could raise T_K in the cold, dense inner region. Goldsmith (2001), Doty & Neufeld (1997), and Lee et al. (2004) found that the effect is relatively small because of efficient gas-dust coupling at the high densities where CO is significantly depleted; therefore, we did not include depletion and desorption in our gas energetics calculation.

The calculated $T_K(r)$ is shown in Figure 8. The gas temperature decreases in less dense regions where gas-dust collisions are not as efficient, but rises at the outer edge because of PE heating. In the gas energetics code, the strength of the UV field relative to the local ISRF on the outside of the core is parameterized as G_0. We use the equation $G_0 = \exp(-1.8 A_V)$, where the attenuation of the ISRF corresponds to a certain external A_V. In dust models, different combinations of external A_V and $s_{\rm ISRF}$ can provide similar fits. For example, Figure 7(c) shows that models with $A_V = 0.4$ with $s_{\rm ISRF} = 4$, $A_V = 1$ with $s_{\rm ISRF} = 5$, and $A_V = 1.5$ with $s_{\rm ISRF} = 6$ result in similar modeled fluxes at 160 μm. However, the calculated gas temperature profile is more sensitive to the external A_V since the attenuation of the ISRF predominately affects the short wavelengths which are important to the PE heating rate. To examine the model temperature at the outer layer and constrain the amount of surrounding extinction, we modeled the CO(2–1) line toward L43E and compare with the observations (Figure 9), and derive the best-fit G_0 of 0.165 (corresponds to an external A_V of 1). Also, the cooling rate depends on the linewidth of CO, and we use a microturbulent width of 0.24 km s^{-1}determined by the C^{18}O line fitting. A more detailed treatment of the line modeling is described in Section 4.4.

4.3. Chemical Models

We use the evolutionary chemical model presented by Lee et al. (2004). A sequence of BE spheres with increasing central densities and an inside-out collapse initiated at the point of a singular isothermal sphere are combined to describe the dynamics, and the model calculates gas and dust temperatures and follows chemical evolution self-consistently at each time step. The collapse model is adopted from Young & Evans (2005) for the evolution of luminosity and density distribution. For RNO91, we use the physical parameters that best match the dust modeling results in Section 4.1, and $r_{\rm inf}$ of 0.006 pc corresponds to the time step of 25000 yr. For L43E, since there is no good constraint for the timescales and dynamics of the PPC stage, we simply assume eight steps of different central densities and test different timescales for each step to optimize the fitting at $n_c = 3 \times 10^5$ cm^{-3}. In the chemical models, we assume bare SiO_2 for dust grain surfaces to which molecules freeze (Bergin et al. 1995).

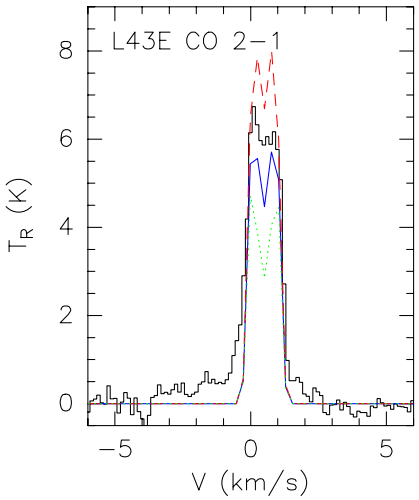

Figure 9. Simple CO line models with the results in Figure 7. The blue line is from the model with $s_{\rm ISRF} = 5$ and $A_V = 1$, the dashed red line is from the model with $s_{\rm ISRF} = 4$ and $A_V = 0.5$, and the dotted green line is from the model with $s_{\rm ISRF} = 4$ and $A_V = 1.5$. X(CO) is assumed 3×10^{-5} in the models, but a higher or lower value only affects the size of the self-absorption dip. The modeled line velocity is shifted to 0.5 km s^{-1} to be aligned with the observed line. The blue wing in the observed CO line profile might come from another component in the cloud.

4.4. Line Modeling

With the best-fit density profile from dust models, the gas temperature profiles from the gas-energetics calculation, and molecular abundances ($X(r)$) from chemical models, the molecular excitation was modeled with a Monte Carlo radiative transfer code (mc) which runs with 40 shells calculating the level populations. We then simulate the observations with a virtual telescope program (vt; Choi et al. 1995) at the observed offset position. We use the $v_{\rm LSR}$ derived from observations for the modeled line velocity in each source. To fit the observed lines, we also use simple abundance profiles, such as constant and step function, to compare with the results from chemical models. The goodness of a fit is determined by eye.

We use collision rates by Flower & Launay (1985) for CO, by Green (1991) for H_2CO, by Flower (1999) for HCO^+, and Daniel et al. (2005) for N_2H^+. For the deuterated species DCO^+, we use the de-excitation rate coefficients of HCO^+, and the excitation rate coefficients are obtained by detailed balance. In some cases, rates are linearly extrapolated to lower temperatures. For N_2H^+ and $C^{17}O$, the components of the hyperfine structures are partially resolved. Components separated by less than the $1/e$ width of the velocity dispersion were aggregated into a single component. The aggregated components are modeled independently with relative intensity-weighted abundances and added together to make combined line profiles.

5. MODELING RESULTS

The line modeling results are presented with the observations in Figure 3. The abundance profiles from chemical models are presented in Figure 10. Some of our line models show self-absorption features, which are not seen in the observed line profiles, especially in HCO^+, H_2CO, and N_2H^+. An explanation for the lack of self-absorption in molecular lines is clumpy cloud

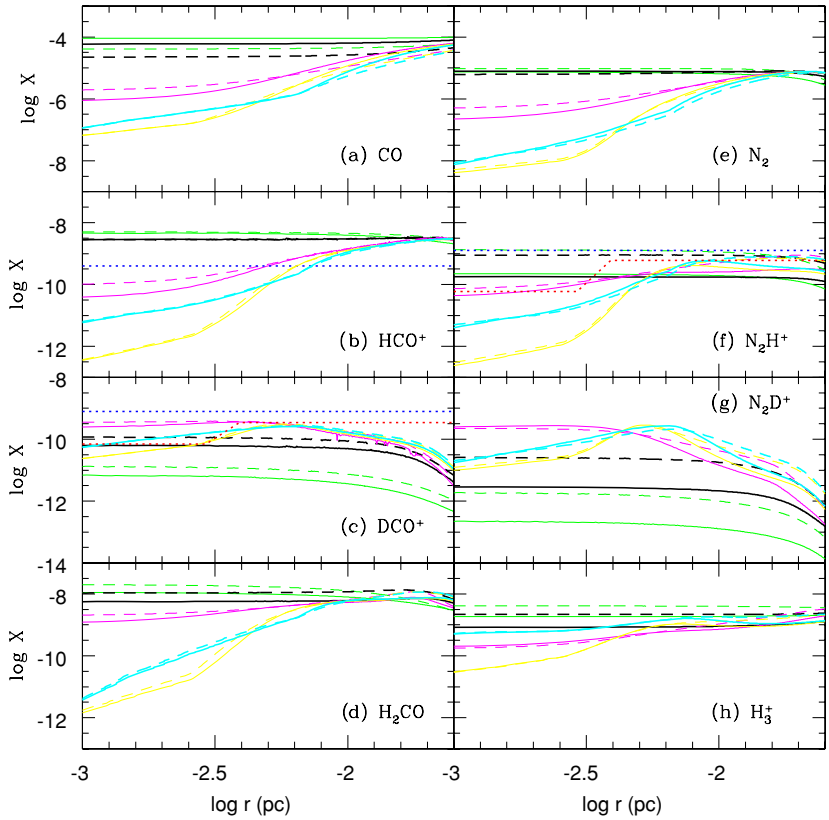

Figure 10. Evolution of abundance profiles for (a) CO, (b) HCO^+, (c) DCO^+, (d) H_2CO, (e) N_2, (f) N_2H^+, (g) N_2D^+, and (h) H_3^+ at selected time steps of Model 1 (solid lines) and Model 2 (dashed lines). The difference between the two models is that Model 2 has a longer PPC timescale. For t < 0 (before collapse), the lines shows BE spheres of central densities 10^5 (green), 3×10^5 (black), and 10^7 (magenta) cm^{-3}. The central densities correspond to different time steps in each model, and the time steps are listed in Table 4. For t > 0 (after collapse), the time steps are $t = 10^4$ (yellow) and $t = 2.5 \times 10^5$ (cyan) yr. The blue dotted lines are best-fit empirical models for HCO^+, DCO^+, and N_2H^+ in L43E. The red dotted lines are best-fit empirical models for DCO^+ and N_2H^+ in RNO91.

Table 4
Chemical Models

Central Density (cm^{-3})	Model 1 Time step (yr)	Model 2 Time step (yr)
10^7	5×10^3	3×10^3
3×10^6	1×10^4	5×10^3
10^6	2×10^4	1.2×10^4
3×10^5	3×10^4	3×10^4
10^5	6×10^4	10^5
3×10^4	1.25×10^5	3.5×10^5
10^4	2.5×10^5	1.5×10^6
10^{3a}	2.5×10^5	1.5×10^6

Note. [a] The initial constant density.

structure with the existence of macroturbulent motions, which is simulated with the Monte Carlo methods for three-dimensional clouds by Juvela (1997). The line profiles can be confused with heavy self-absorption as well as rotation (e.g., Pavlyuchenkov et al. 2008). Since we are not including a complete three-dimensional calculation in this paper, we only fit the line strength at half maximum level for lines that are self-absorbed in the models.

From observations toward star forming cores, one of the features that potentially indicates the evolutionary status is an anti-correlation of CO and N_2H^+. N_2H^+ is thought to be a good tracer of dense core gas at earlier evolutionary stages until T_D reaches the temperature for CO evaporation. The relative depletion and desorption of N_2 and CO are the key processes governing the abundance of N_2H^+; however, recent laboratory result shows there is no significant difference of N_2 and CO binding energies (Öberg et al. 2005; Bisschop et al. 2006). With an updated higher value of N_2 binding energies, the modeled N_2H^+ lines are much weaker than the observed lines. The timescale for the PPC stage is also a key issue for the freeze-out of molecules, so we varied the timescales at different central densities. A longer total timescale allows more N_2 to form, but a longer time at higher densities ($n > 10^5$ cm^{-3}) would result in more depletion. N_2H^+ abundances are directly affected by the amount of N_2 formation and CO depletion. To fit the observed N_2H^+ lines, we assume a longer total timescale that allows more N_2 formation and CO depletion and shorter time at later stages to prevent N_2 depletion. Two test models are listed in Table 4. We use the timescales in Lee et al. (2004) as the standard model (Model 1), and to optimize the N_2H^+ abundances for L43E, a longer total timescale of 2×10^6 yr is assumed (Model 2). In Figure 10, the solid lines are abundance profiles from Model 1, and the dashed lines are from Model 2. For both models, we also tested the N_2H^+ dissociative recombination rates in Geppert et al. (2004) to compare with the rates in the UMIST database for astrochemistry 1999 (Le Teuff et al. 2000). The rates in Geppert et al. (2004) fit the observations better, and are included in our chemical network for the models presented in this paper.

The CO lines are difficult to fit in detail since they are very optically thick and confused by the wing components. The line profile toward RNO91 has wide outflow wings, and the line profile toward L43E also shows a blue wing which possibly comes from another component in the foreground along the line of sight. The modeled CO abundances can still be tested through line fitting of CO isotopologues. We assume the abundance profiles for the CO isotopologues have the same form as CO with an isotope ratio of $O/^{18}O = 580$ (Wilson & Rood 1994) and $^{18}O/^{17}O = 4$ (Wouterloot et al. 2005). In Model 2, the modeled $C^{18}O$ and $C^{17}O$ line intensities are efficiently decreased to fit the data since more CO depletion is produced. We also assume an ortho to para ratio of 1.5 (Dickens & Irvine 1999) to model the ortho-H_2CO ($3_{1,2} - 2_{1,1}$) lines. For L43E, the H_2CO abundance in Model 2 is higher than in Model 1 by a factor of 2, but it is possible that self-absorption has greatly weakened the blue peak.

For the HCO^+ lines toward L43E, although the observed line profile might be obscured by absorption from a foreground component, the modeled line is still too strong. The cosmic ray ionization rates could affect the results, but neither enhanced nor lowered reaction rates improved the fit of both HCO^+ and N_2H^+ data in both cores simultaneously. We tested empirical abundance profiles with lower abundance at large radii. For example, if G_0 is higher than we adopted, the higher dissociative recombination rate can lower the abundance in the outer region. However, we did not find an improved fit even with extremely low HCO^+ abundances in the outer region. To match the line intensity according to the red peak, we use a constant abundance $X(HCO^+) = 4 \times 10^{-10}$, which is lower than the chemical model prediction by a factor of ~7.5. For the deuterated species, since they are favored in a cold region with CO depletion, both DCO^+ and N_2D^+ are enhanced relative to HCO^+ and N_2H^+ at high densities. The DCO^+ abundances in L43E are increased from Model 1 to Model 2 because of the amount of CO depletion, but the modeled DCO^+ lines from chemical models are still weaker than observed. The DCO^+ line emission generated primarily in the center region with high densities where HCO^+ can be depleted. It is possible that there is still more CO depletion than the chemical models predict. A DCO^+ abundance increased by a factor of ~8 is needed to fit the observed line intensity for L43E, and for RNO91, we use a step function with depletion factor of 5 within 0.003 pc. The best-fit empirical abundance profiles are shown in Figure 10 with blue dotted lines for L43E and red dotted lines for RNO91. To compare with the results in Section 3.3.3, we also calculated the optical depths for the best-fit HCO^+ lines with empirical abundances. The optical depth of the simulated HCO^+(3-2) line in RNO91 is 23, which is much higher than the value of 3 in L43E. This result also supports the analysis in Section 3.3.3 that the $N(DCO^+)/N(HCO^+)$ factors calculated with optically thin approximation provide a lower limit, with $N(DCO^+)/N(HCO^+)$ at least 4.8 times more enhanced in L43E than in RNO91.

To summarize, most of the lines in both sources can be fitted reasonably well with Model 2, which has a longer timescale for the PPC stage. However, the change of parameters in our different chemical models may only be compensating the effects not yet included. For example, the grain properties should also be time-dependent. Grain mantles covered by water-rich ice have strong binding energies for molecules to freeze on, but N_2 forms slowly and is less affected. As the density increases and CO freezes out, the grain mantle surfaces can be contaminated by CO ice. Once grain mantles are CO-dominant, the binding energies are lower, which results in less depletion of N_2 and N_2H^+ compared with HCO^+, since HCO^+ depletion follows CO depletion. Our modeling results of longer timescales at low densities may work equivalently to the effects of higher grain surface binding energies (water-dominant) at lower densities. The difference between our modeling results and observations may be more specifically explained in a model including time-dependent grain properties. Heavy CO (and thus HCO^+)

depletion on the initial water-dominant grain surfaces can result in more abundant DCO^+. With time, grain surfaces are covered with CO (which produces CO_2 on surface), resulting in less depletion of N_2 and more abundant N_2H^+.

6. SUMMARY

We have presented *Spitzer* observations and molecular line observations from the CSO toward the two sources RNO91 and L43E evolving in the same region. A self-consistent modeling procedure is employed to investigate the physical condition in each source, and to compare the chemistry in an evolutionary picture. Our results are as follows.

From the *Spitzer* images, RNO91 can be categorized as Class I, and L43E is still starless with no embedded source detected. CO depletion is seen in both sources, but the degree of depletion is higher in L43E. Also, strong DCO^+ enhancement is seen in L43E.

Dust modeling results showed that L43E can be fitted by a BE sphere with central density of 3×10^5 cm^{-3}, and RNO91 is characterized to have $r_{\rm inf}$ of 0.006 pc with an inside-out collapse model (Shu 1977). For the line modeling, the best-fitting chemical model suggests a longer total timescale at earlier stages but fast evolution at higher densities for the PPC stage. The observed abundances of N_2H^+ and CO isotopologues can be matched well in both sources, but in L43E, the modeled HCO^+ abundance is too high by a factor of 7.5, and the modeled DCO^+ abundance is too low by a factor of 8. It is possible there is still more CO depletion in the center than the model predicted. In this picture, RNO91 is possibly the first star forming in this region, and L43E could be spending a longer time at the PPC phase.

We thank Yancy Shirley for providing the radial intensity profiles from the SCUBA data, Jingwen Wu, Michael Dunham, Miranda Dunham, and Hyo Jeong Kim for their help to obtain the data at the CSO, and Ted Bergin for the chemical code. Support for this work, part of the Spitzer Legacy Science Program, was provided by NASA through contract 1224608 issued by the Jet Propulsion Laboratory, California Institute of Technology, under NASA contract 1407. This work has also been supported by NSF Grants AST-0307250, AST-0607793, NASA Origins grant NNX07AJ72G, the National Research Foundation of Korea (NRF) government (MEST) (No. 2009-0062865), and supported in part by a grant (R01-2007-000-20336-0) from the Basic Research Program of the KOSEF.

REFERENCES

Aikawa, Y., Herbst, E., Roberts, H., & Caselli, P. 2005, ApJ, 620, 330
Allen, L. E., et al. 2004, ApJS, 154, 363
André, P., & Montmerle, T. 1994, ApJ, 420, 837
André, P., Ward-Thompson, D., & Barsony, M. 1993, ApJ, 406, 122
Bergin, E. A., Langer, W. D., & Goldsmith, P. F. 1995, ApJ, 441, 222
Bisschop, S. E., Fraser, H. J., Öberg, K. I., van Dishoeck, E. F., & Schlemmer, S. 2006, A&A, 449, 1297
Black, J. H. 1994, in ASP Conf. Ser. 58, The First Symposium on the Infrared Cirrus and Diffuse Interstellar Clouds, ed. R. M. Cutri & W. B. Latter (San Francisco, CA: ASP), 355
Boogert, A. C. A., et al. 2008, ApJ, 678, 985
Caselli, P., Walmsley, C. M., Tafalla, M., Dore, L., & Myers, P. C. 1999, ApJ, 523, L165
Caselli, P., Walmsley, C. M., Zucconi, A., Tafalla, M., Dore, L., & Myers, P. C. 2002, ApJ, 565, 344
Chen, H., Myers, P. C., Lad, d E. F., & Wood, D. O. S. 1995, ApJ, 445, 377
Choi, M., Evans, N. J., II, Gregersen, E. M., & Wang, Y. 1995, ApJ, 448, 742
Crapsi, A., Caselli, P., Walmsley, C. M., Myers, P. C., Tafalla, M., Lee, C. W., & Bourke, T. L. 2005, ApJ, 619, 379
Crapsi, A., van Dishoeck, E. F., Hogerheijde, M. R., Pontoppidan, K. M., & Dullemond, C. P. 2008, A&A, 486, 245
Daniel, F., Dubernet, M.-L., Meuwly, M., Cernicharo, J., & Pagani, L. 2005, MNRAS, 363, 1083
de Geus, E. J., de Zeeuw, P. T., & Lub, J. 1989, A&A, 216, 44
Dalgarno, A., & Lepp, S. 1984, ApJ, 287, L47
Dickens, J. E., & Irvine, W. M. 1999, ApJ, 518, 733
Dickman, R. L. 1978, ApJS, 37, 407
Doty, S. E., & Neufeld, D. A. 1997, ApJ, 489, 122
Draine, B. T. 1978, ApJS, 36, 595
Draine, B. T., & Lee, H. M. 1984, ApJ, 285, 89
Draine, B. T. 2003, ARA&A, 41, 241
Egan, M. P., Leung, C. M., & Spagna, G. R. 1988, Comput. Phys. Commun., 48, 271
Evans, N. J., II, Lee, J.-E., Rawlings, J. M. C., & Choi, M. 2005, ApJ, 626, 919
Evans, N. J., II, Rawlings, J. M. C., Shirley, Y. L., & Mundy, L. G. 2001, ApJ, 557, 193
Evans, N. J., II, et al. 2003, PASP, 115, 965
Evans, N. J., II, et al. 2007, Final Delivery of Data from the c2d Legacy Project: IRAC and MIPS (Pasadena, CA: SSC), http://ssc.spitzer.caltech.edu/legacy/c2dhistory.html
Fazio, G. G., et al. 2004, ApJS, 154, 10
Flower, D. R. 1999, MNRAS, 305, 651
Flower, D. R., & Launay, J. M. 1985, MNRAS, 214, 271
Geppert, W. D., et al. 2004, ApJ, 609, 459
Goldsmith, P. F. 2001, ApJ, 557, 736
Green, S. 1991, ApJS, 76, 979
Harvey, P., et al. 2006, ApJ, 644, 307
Hodapp, K-W. 1994, ApJS, 94, 615
Jørgensen, J. K. 2004a, A&A, 424, 589
Jørgensen, J. K., Schoier, F. L., & van Dishoeck, E. F. 2004b, A&A, 416, 603
Juvela, M. 1997, A&A, 322, 943
Kirk, J. M., Ward-Thompson, D., & André, P. 2005, MNRAS, 360, 1506
Lacy, J. H., Knacke, R., Geballe, T. R., & Tokunaga, A. T. 1994, ApJ, 428, L69
Ladd, E. F., Fuller, G. A., & Deane, J. R. 1998, ApJ, 495, 871
Ladd, E. F., et al. 1991, ApJ, 366, L203
Lee, C.-F., & Ho, P. T. P. 2005, ApJ, 624, 841
Lee, C.-F., Mundy, L. G., Stone, J. M., & Ostriker, E. C. 2002, ApJ, 576, 294
Lee, J.-E, Bergin, E. A., & Evans, N. J., II. 2004, ApJ, 617, 360
Lee, J.-E, Di Francesco, J., Bourke, T. L., Evans, N. J., II, & Wu, J. 2007, ApJ, 671, 1748
Lee, J.-E, Evans, N. J., II, & Shirley, Y. L 2003, ApJ, 583, 789
Le Teuff, Y. H., Millar, T. J., & Markwick, A. J. 2000, A&AS, 146, 157
Lynds, B. T. 1962, ApJS, 7, 1
Mathieu, R. D., Myers, P. C., Schild, R. E., Benson, P. J., & Fuller, G. A. 1988, ApJ, 330, 385
Myers, P. C., Fuller, G. A., Mathieu, R. D., Beichman, C. A., Benson, P. J., Schild, R. E., & Emerson, J. P. 1987, ApJ, 319, 340
Öberg, K. I., van Broekhuizen, F., Fraser, H. J., Bisschop, S. E., van Dishoeck, E. F., & Schlemmer, S. 2005, ApJ, 621, L33
Oliveira, C. M., Hebrard, G., Howk, J. C., Kruk, J. W., Chayer, P., & Moos, H. W. 2003, ApJ, 587, 235
Ossenkopf, V., & Henning, Th. 1994, A&A, 291, 943
Pavlyuchenkov, Ya., Wiebe, D., Shustov, B., Henning, Th., Launhardt, R., & Semenov, D. 2008, ApJ, 689, 335
Rieke, G. H., et al. 2004, ApJS, 154, 25
Robitaille, T. P., Whitney, B. A., Indebetouw, R., Wood, K., & Denzmore, P. 2006, ApJS, 167, 256
Shirley, Y. L., Evans, N. J., II, & Rawlings, J. M. C. 2002, ApJ, 575, 337
Shirley, Y. L., Evans, N. J., II, Rawlings, J. M. C., & Gregersen, E. M. 2000, ApJS, 131, 249
Shu, F. H. 1977, ApJ, 214, 488
Stutz, A. M., et al. 2007, ApJ, 665, 466
Tafalla, M., Myers, P. C., Caselli, P., & Walmsley, C. M. 2004, A&A, 416, 191
Tafalla, M., Myers, P. C., Caselli, P., Walmsley, C. M., & Comito, C. 2002, ApJ, 569, 815
van der Tak, F. F. S., van Dishoeck, E. F., Evans, N. J., II, & Blake, G. A. 2000, ApJ, 537, 283
Ward-Thompson, D., Scott, P. F., Hills, R. E., & André, P. 1994, MNRAS, 268, 276
Ward-Thompson, D., Motte, F., & André, P. 1999, MNRAS, 305, 143

Weintraub, D. A., Tegler, S. C., Kastner, J. H., & Rettig, T. 1994, ApJ, 423, 674
Whitney, B. A., Wood, K., Bjorkman, J. E., & Cohen, M. 2003a, ApJ, 598, 1079
Whitney, B. A., Wood, K., Bjorkman, J. E., & Wolff, M. J. 2003b, ApJ, 591, 1049
Wilson, T. L., & Rood, R. T. 1994, ARA&A, 32, 191
Wouterloot, J. G. A., Brand, J., & Henkel, C. 2005, A&A, 430, 549
Wu, J., Dunham, M. M., Evans, N. J., II, Bourke, T. L., & Young, C. H. 2007, AJ, 133, 1560
Young, C. H., & Evans, N. J., II. 2005, ApJ, 627, 293
Young, C. H., et al. 2006, AJ, 132, 1998
Young, K. E., Lee, J.-E., Evans, N. J., II, Goldsmith, P. F., & Doty, S. D. 2004, ApJ, 614, 252
Young, K. E., et al. 2005, ApJ, 628, 283